

Effective reaction temperatures of irreversible dust chemical reactions in a protoplanetary disk

Lily Ishizaki^{1,2}, Shogo Tachibana², Tamami Okamoto³, Daiki Yamamoto⁴, Shigeru Ida³

Running head: Effective reaction temperatures of dust chemical reactions

ABSTRACT

Dust particles in protoplanetary disks experience various chemical reactions under different physicochemical conditions through their accretion and diffusion, which results in the radial chemical gradient of dust. We performed three-dimensional Monte Carlo simulations to evaluate the dust trajectories and the progress of fictitious irreversible reactions, of which kinetics is expressed by the Johnson-Mehl-Avrami equation. The distribution of the highest temperature that each particle experiences before the degree of reaction exceeds a certain level shows the log-normal distribution, and its mode temperature was used as the effective reaction temperature. Semi-analytical prediction formulas of the effective reaction temperature and its dispersion were derived by comparing a reaction timescale with a diffusive transport timescale of dust as a function of the reaction parameters and the disk parameters. The formulas reproduce the numerical results of the effective reaction temperatures and their dispersions within 5.5 and 24 %, respectively, in a wide temperature range (200–1400 K). We applied the formulas for the crystallization of amorphous silicate dust and its oxygen isotope exchange with the H₂O vapor based on the experimentally determined kinetics. For sub-micron sized amorphous forsterite dust, the predicted effective reaction temperature for the oxygen isotope exchange was lower than that of crystallization without overlap even considering their dispersions. This suggests that the amorphous silicate dust in the protosolar disk could exchange their oxygen isotopes efficiently with the ¹⁶O-poor H₂O vapor, resulting in the distinct oxygen isotope compositions from the Sun.

¹ Corresponding author r.ishizaki@eps.s.u-tokyo.ac.jp

² Department of Earth and Planetary Science, The University of Tokyo, Hongo, Tokyo 113-0033, Japan

³ Earth-Life Science Institute, Tokyo Institute of Technology, Meguro, Tokyo 152-8550, Japan

⁴ Department of Earth and Planetary Sciences, Kyushu University, Motoooka, Nishi-ku, Fukuoka 819-0395, Japan

1. INTRODUCTION

Various dust chemical reactions occur in a protoplanetary disk depending on physicochemical conditions that dust experiences through its accretional and diffusive transport. Such chemical reactions would be responsible for making the chemical diversity of dust in the disk.

Chemical reactions of dust moving in protoplanetary disks have been modeled using Monte Carlo simulations to simulate the diffusive random motion of dust (e.g., Ciesla 2011; Ciesla & Sandford 2012; Okamoto & Ida 2022). Ciesla (2011) developed the Monte Carlo simulation of dust particles movement in an accreting protoplanetary disk to show that crystalline silicate particles initially at ~ 5 au can diffuse out to the region beyond 20 au, suggesting that dust experiencing a certain temperature for complete crystallization can be incorporated into comets that formed well beyond the snow line. With the same 3D Monte Carlo simulation, Ciesla and Sandford (2012) demonstrated that amorphous ice dust is stirred up above the disk photo-surface long enough and accumulation of radicals in the dust by UV photon irradiation produces complex organic molecules in a protoplanetary disk.

Okamoto and Ida (2022) discussed the redistribution of silicate dust particles that crystallize at the crystallization line (~ 1000 K) in a protoplanetary disk using the 3D Monte Carlo simulation. Considering the pebble accretion model (e.g., Lambrechts & Johansen 2014) and assuming that the pebbles consist of many small amorphous silicate particles embedded in the icy mantle, they adopted the simulation setting that the small-sized silicate particles are released by ice sublimation at the snow line (e.g., Saito & Sirono 2011; Morbidelli et al. 2015; Ida & Guillot 2016). Because they consistently simulated the trajectories of both particles that once moved into the region with > 1000 K to be crystallized and those staying in amorphous structure, they quantitatively calculated crystallization ratio of silicate dust particles that diffuse out to the outer region of the disk to be incorporated in comets, although the estimated fraction of crystalline dust is a few times smaller than the observation, as long as the amorphous silicate dust is continuously supplied by icy pebbles.

These previous studies focused on specific reactions of dust in the accretion disk, but various dust chemical reactions occur under protoplanetary disk conditions, which should contribute to the chemical evolution of the disk. The difference in critical reaction temperatures should thus be responsible for making the radial chemical gradient of dust. Because the dust moves advectively and diffusively in the accretion disk, the chemical reaction of dust should be discussed with its kinetics that has a strong temperature dependence.

In this work, we aim to determine critical reaction temperatures of various irreversible chemical reactions of dust in a steady accretion disk and obtain the general expression of the reaction temperatures as a function of both reaction and disk parameters.

In the next section, we describe the protoplanetary disk model, the 3D Monte Carlo simulation method to track trajectories of dust particles and their chemical reactions. Section 3 shows the results of the simulations focusing on the highest temperature that dust experience until the reaction degree reaches a certain level. Section 4 discusses the semi-analytical general formula of the effective reaction temperature. We apply the formula for the reaction temperatures of crystallization and oxygen isotope exchange of amorphous silicate dust and discuss its cosmochemical implication in Section 5, followed by the conclusion in Section 6.

2. METHOD

2.1. Disk Model

In this work, we simulated irreversible chemical reactions of dust particles moving advectively and diffusively in a steady accretion disk around a solar-mass central star (M_{\odot}) using the 3D Monte Carlo simulation (e.g., Ciesla 2011; Ciesla & Sandford 2012; Okamoto & Ida 2022).

We adopted a steady accretion disk with a mass accreting rate of \dot{M} . Diffusivity of dust, D , is given as the gas turbulent viscosity, $\nu_{\text{vis}} = \alpha c_s H$, where α is a dimensionless viscous parameter ($0 < \alpha \leq 1$), H is the local gas scale height, and c_s is the local speed of sound (the α -viscosity model; Shakura & Sunyaev 1973).

The accreting disk is heated by uniform viscous heating, proportional to the local gas spatial density. We assumed that the disk is in hydrostatic equilibrium such that $\rho(z) = (\Sigma_g / \sqrt{2\pi}H) \exp(-z^2/2H^2)$ in the vertical direction, where Σ_g is the disk gas surface density and z is the height. The optical depth at z is calculated as

$$\tau_z \equiv \int_{|z|}^{\infty} \kappa \rho(z) dz = \frac{\kappa \Sigma_g}{\sqrt{\pi}} \int_{z/\sqrt{2}H}^{\infty} \exp(-x^2) dx = \frac{\kappa \Sigma_g}{2} \left[1 - \operatorname{erf}\left(\frac{z}{\sqrt{2}H}\right) \right], \quad (1)$$

where κ is the opacity, and $\operatorname{erf}(x)$ is the error function:

$$\operatorname{erf}(x) \equiv \frac{2}{\sqrt{\pi}} \int_x^{\infty} \exp(-x'^2) dx'. \quad (2)$$

The opacity is assumed to be $\kappa = 2.5 \text{ cm}^2/\text{g}$ (e.g., Pollack et al., 1985, 1994). We here note that the value of κ changes the thermal structure of the disk, but we found that it does not affect the discussion on the effective reaction temperatures in the range of $\kappa=1\text{--}4 \text{ cm}^2/\text{g}$.

The photo-surface temperature of the disk is given by

$$T_{\text{surf}} \simeq 85 \left(\frac{\dot{M}}{10^{-8} M_{\odot}/\text{yr}} \right)^{1/4} \left(\frac{r}{1\text{au}} \right)^{-3/4}. \quad (3)$$

and temperature at z is given by

$$T(z) = \left[1 + \frac{3(\tau_z - 1)}{4} \left(1 - \frac{\tau_z - 1}{\tau_{\text{disk}}} \right) \right]^{1/4} T_{\text{surf}}, \quad (4)$$

where τ_{disk} is the disk optical depth, defined by

$$\tau_{\text{disk}} \equiv \int_{-\infty}^{\infty} \kappa \rho(z) dz. \quad (5)$$

The derivation of Eq. (4) is given in Appendix. In the analytical derivation of the midplane temperature from T_{surf} , it is often assumed that the viscous heating is concentrated at $z = 0$ (Lin & Papaloizou 1985). However, because chemical reactions generally have sensitive temperature dependences, we use the disk temperature as a continuous function of z given by Eq. (4) with the assumption that viscous heating rate is proportional to $\rho(z)$. The temperature gradient along the z direction was not included in previous studies (Ciesla 2011; Ciesla & Sandford 2012; Okamoto & Ida 2022), and its effect on the reaction progress will be discussed below.

The steady mass accretion rate is given by $\dot{M} \simeq 3\pi \Sigma_g \nu_{\text{vis}}$, and the gas surface density is expressed as

$$\Sigma_g \simeq 165 \left(\frac{\alpha}{10^{-2}} \right)^{-4/5} \left(\frac{\dot{M}}{10^{-8} M_\odot \text{ yr}^{-1}} \right)^{3/5} \left(\frac{r}{1 \text{ au}} \right)^{-3/5} \text{ g/cm}^2. \quad (6)$$

At the midplane where $z = 0$ and $t_z = t_{\text{disk}}/2 = \kappa \Sigma_g/2$, the disk temperature $t_{\text{disk}} \gg 1$ is given by

$$T_c \simeq \left(\frac{3 \tau_{\text{disk}}}{16} \right)^{1/4} T_{\text{surf}} \simeq 607 \left(\frac{\alpha}{10^{-2}} \right)^{-1/5} \left(\frac{\dot{M}}{10^{-8} M_\odot \text{ yr}^{-1}} \right)^{2/5} \left(\frac{r}{1 \text{ au}} \right)^{-9/10}. \quad (7)$$

2.2. Trajectories of Dust Particles

Following Ciesla (2010, 2011), we performed 3D Monte Carlo simulations to evaluate the trajectories of dust particles in the steady-state accretion disk. Dust size was assumed to be small enough to be well coupled with gas. The 3D Monte Carlo Lagrangian simulation model reproduces the surface density evolution of dust particles following the Eulerian advection-diffusion equation (Ciesla 2010, 2011):

$$\frac{\partial \Sigma_d}{\partial t} = \frac{1}{r} \frac{\partial}{\partial r} \left[r \Sigma_d \left(v_r - \frac{D}{\Sigma_d / \Sigma_g} \frac{\partial}{\partial r} \left(\frac{\Sigma_d}{\Sigma_g} \right) \right) \right], \quad (8)$$

where Σ_d is the surface density of dust and v_r is their radial advection velocity (e.g., Okamoto & Ida 2022). The motions of an individual particle are described by

$$x_i = x_{i-1} + v_x \delta t_{\text{phys}} + \mathcal{R}_x \sqrt{6D(x') \delta t_{\text{phys}}}, \quad (9)$$

$$y_i = y_{i-1} + v_y \delta t_{\text{phys}} + \mathcal{R}_y \sqrt{6D(y') \delta t_{\text{phys}}}, \quad (10)$$

$$z_i = z_{i-1} + v_z \delta t_{\text{phys}} + \mathcal{R}_z \sqrt{6D(z') \delta t_{\text{phys}}}, \quad (11)$$

Where δt_{phys} is the timestep to calculate trajectories, $\delta t_{\text{phys}} = \Omega_K^{-1}$, where Ω_K is the local Keplerian frequency, and \mathcal{R}_x , \mathcal{R}_y , and \mathcal{R}_z are independent random numbers with a value between -1 and 1 . The second and third terms on the right represent advection and diffusion, respectively. Accounting for gradients in the diffusivity, x' , y' , and z' are given by $x' = x_{i-1} + (\partial D / \partial x)/2$, $y' = y_{i-1} + (\partial D / \partial y)/2$, and $z' = z_{i-1} + (\partial D / \partial z)/2$ (e.g., Visser, 1997; Ciesla, 2010). The advection velocities of dust accreting with gas in the steady accretion disk are given by

$$v_x = v_{\text{drag},r} \times \frac{x}{r}, \quad (12)$$

$$v_y = v_{\text{drag},r} \times \frac{y}{r}, \quad (13)$$

$$v_z = v_{\text{drag},z} + \partial D(z) / \partial z - \alpha \Omega_K z, \quad (14)$$

where x , y , and z are the values of the Cartesian coordinates, and r is the radial distance from the central star, given by $r = \sqrt{x^2 + y^2}$. In this well-coupled case, the radial velocity is given by $v_{\text{drag},r} = v_r = -3n_{\text{vis}}/2r = -(3/2)\alpha (H/r)^2 v_K$, where v_K is the local Keplerian velocity. Because $v_{\text{drag},z} = 0$ and $\partial D(z) / \partial z = \partial v_{\text{vis}} / \partial z = 0$, $v_z = -\alpha \Omega_K z$. To check the validity of the simulation, we made the same dust trajectory calculation with those in previous studies (Ciesla 2010, 2011; Okamoto & Ida 2022), and confirmed that our trajectory calculations give the consistent results with previous studies.

In the simulations, 10^4 dust particles were released at the disk midplane near the H₂O snowline ($T \approx 180$ K) for each disk parameter set (see Section 2.4), according to the simulation setting adopted by Okamoto and Ida (2022). Because we do not consider collective effects, back-reaction from dust to gas nor dust growth, the dust particle trajectories are independently integrated. The calculations continued for up to 10^6 years. We note here that this initial location has almost no effect on the estimate of the reaction temperatures as long as they occur at >200 K.

2.3. Reaction Kinetics

Progresses of many irreversible chemical reactions are well described empirically by the Johnson-Mehl-Avrami (JMA) equation (Avrami 1939; Johnson & Mehl 1939):

$$X = 1 - \exp\left[-\left(\frac{t}{\tau}\right)^n\right], \quad (15)$$

where X is the degree of each reaction, t is time, and n is the Avrami index. The time evolution of X is represented by the sigmoidal-shaped curve, resulting in slowing the reaction rate before completion. Therefore, this empirical equation implicitly includes the reduction of the driving force of reaction when the reaction approaches the equilibrium.

The characteristic reaction timescale, τ , is given by

$$\tau = \left[v_{\text{chem}} \exp\left(-\frac{E_a}{RT}\right) \right]^{-1}, \quad (16)$$

where v_{chem} is the pre-exponential factor, E_a is the activation energy, and R is the gas constant. The reaction parameters n , v_{chem} , and E_a can be determined by laboratory experiments.

We note here that the dependence of kinetic parameters on the disk gas density and/or gas chemistry is not considered for simplicity although their dependence on the gas chemistry has been reported in some cases (e.g., crystallization of amorphous silicate with the composition of Mg₂SiO₄; Yamamoto and Tachibana, 2018). We do not consider reversible chemical reactions such as evaporation and condensation of dust, whose kinetics is not expressed simply by Eq. 16 (e.g., Takigawa et al., 2009; Tachibana et al., 2011; Takigawa et al., 2015), either. The driving force of the reaction (Gibbs energy change of the reaction ΔG) depends on the degree of progress of reversible reactions, and in some cases is a function of gas density (e.g., evaporation of minerals in hydrogen gas: Tachibana and Tsuchiyama, 1998; Tsuchiyama et al., 1999; Tachibana et al., 2002; Takigawa et al., 2009). These reactions are also important targets for future work.

We simulated the progress of fictitious chemical reactions of dust moving in the disk as described in Section 2.2. In the simulation, X is set to zero when the dust is released at the snowline. For each timestep of the Monte Carlo simulation, the increment δX is calculated by the following differentiated JMA equation with local T at the position of the particle:

$$\delta X = (1 - X) \left(1 - \exp\left(-n \frac{\delta t_{\text{chem}}}{\tau} (-\ln(1 - X))^{1-\frac{1}{n}}\right) \right). \quad (17)$$

Because the chemical reaction has a strong temperature dependence, the reaction may proceed significantly during the physical timestep δt_{phys} depending on the reaction parameters and the temperature. To prevent such an abrupt reaction

progress during δt_{phys} , we newly introduced the chemical timestep δt_{chem} . The chemical time step is defined as the duration for a reaction to progress with δX_{lim} of 0.01:

$$\delta t_{\text{chem}} = -\frac{n}{\tau(-\ln(1-X))^{1-\frac{1}{n}}} \ln\left(1 - \frac{\delta X_{\text{lim}}}{1-X}\right), \quad (18)$$

and was used when δX is larger than δX_{lim} for a given δt_{phys} (Section 2.2). We assumed that the dust keeps linear motion during δt_{phys} , and the local temperature was updated at each chemical time step δt_{chem} until the sum of δt_{chem} becomes equal to δt_{phys} . Note that δt_{chem} is set equal to δt_{phys} when $\delta X < \delta X_{\text{lim}}$ during δt_{phys} .

2.4. Parameters

The following disk parameters were used for the simulation; the viscous parameter α of 10^{-2} and 10^{-3} (e.g., Sano et al. 2004) and the steady accretion rate \dot{M} of 10^{-6} , 10^{-7} and $10^{-8} M_{\odot} \text{ yr}^{-1}$ (Muzerolle et al. 2000).

In order to simulate a wide variety of chemical reactions (Eq. 16), we surveyed hypothetical reactions with the logarithm of pre-exponential factor of $\ln(\nu_{\text{chem}}[\text{s}^{-1}])$ of 10, 20, 30, 40, 50, and 60, the Avrami index n of 0.5, 1.0, 1.5, 2.5, and 4.0, and the activation energy E_a of 20, 50, 100, 150, 200, 300, 400, 500, 600, 800, and 1000 kJ mol $^{-1}$. These parameters cover various reactions occurring in a wide temperature range (e.g., desorption of chemisorbed molecules, volume diffusion of elements in solids, crystallization of amorphous silicates, gas-solid reactions, and evaporation of minerals) (Tachibana & Tsuchiyama, 1998; Tachibana et al., 2002; Takigawa et al., 2009; Tachibana et al., 2011; Takigawa et al., 2015; Yamamoto & Tachibana, 2018; Kuroda et al., 2018, 2019; Yamamoto et al., 2018, 2020, 2021). We assumed that the reactions are not dependent on the disk gas pressure in this study.

The effective reaction temperature of a chemical reaction is discussed below using the highest temperature ($T_{\text{max}}^{X_{\text{reac}}}$) that each dust particle experiences before the degree of reaction reaches a certain level X_{reac} . The $T_{\text{max}}^{X_{\text{reac}}}$ at X_{reac} of 0.8, 0.9 and 0.99 were recorded for each dust in this study. Because chemical reactions are the most sensitive to temperature as shown in Eq. (16), we are concerned with the highest temperature.

By combining these parameters, we made 5940 3D Monte Carlo simulations (330 reactions \times 6 disk parameters \times 3 X_{reac}).

3. NUMERICAL RESULTS

3.1. Progress of a chemical reaction of dust in the accreting disk

A representative trajectory of a dust particle is shown in Fig. 1(a). The overall trend of dust movement is the inward advection due to accretion, but the diffusive movement due to turbulence is overprinted. In some cases, the outward diffusion of dust also occurs.

Progress of a chemical reaction ($\ln(\nu_{\text{chem}}[\text{s}^{-1}]) = 30$, $E_a = 300 \text{ kJ mol}^{-1}$ and $n = 0.5$) of the same particle is shown in Fig. 1(b) with the temperature that the dust experiences until X reaches 0.99. It is found that the reaction begins to proceed when the dust moves to the region where the temperature is $\sim 600 \text{ K}$. Further advective motion of the dust brings it into the inner higher temperature region, leading to the progress of the reaction. Some horizontal lines in Fig. 1(b) represent a halt of the reaction due to diffusion of the dust upward/downward or outward into the lower temperature region, where the strong temperature dependence of the reaction rate prevents the progress of the reaction. The reaction effectively proceeds when the dust is in the region with temperature of 600-800 K (Fig. 1(b)). The highest temperature that the dust experiences before X reaches $X_{\text{reac}} = 0.99$ ($T_{\text{max}}^{0.99}$) is 793 K, shown with a vertical line in Fig. 1(b).

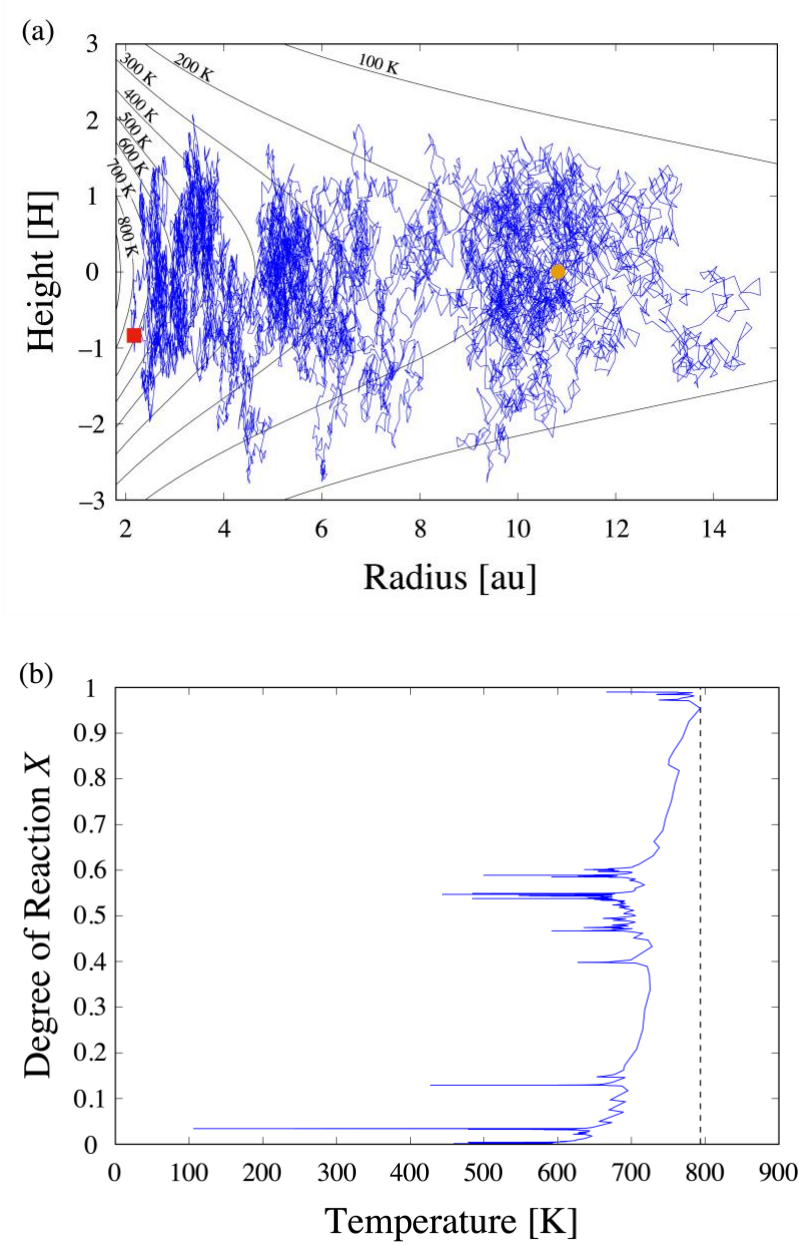


Figure 1. (a) A representative path of a particle that moves in a steady accretion disk with $\alpha=10^{-2}$ and $\dot{M} = 10^{-6} M_{\odot} \text{ yr}^{-1}$. The vertical axis is the disk height z normalized to the scale height H at a given radius. Contour lines show the disk temperature. The particle was released at the orange circle point and completed a reaction ($X_{\text{reac}}=0.99$) at the red square point. (b) A progress of the reaction and a temperature profile of the dust in Fig. 1(a). The reaction parameters are $\ln(\nu_{\text{chem}}[\text{s}^{-1}]) = 30$, $E_a = 300 \text{ kJ mol}^{-1}$ and $n = 0.5$. A vertical line shows the highest temperature $T_{\text{max}}^{0.99}$ that the dust experiences before X reaches X_{reac} of 0.99 (793 K).

3.2. Effective reaction temperatures and their dispersion

We made histograms of $T_{\max}^{X_{\text{reac}}}$ for the particles, of which X exceeds X_{reac} during the simulation. The bin width of the histogram was determined by Scott's choice as $3.5\hat{\sigma}/\sqrt[3]{N}$, where $\hat{\sigma}$ is the standard deviation of $T_{\max}^{X_{\text{reac}}}$ and N is the total number of particles (Scott, 1979). Some examples of the histograms are shown in Fig. 2.

All the $T_{\max}^{X_{\text{reac}}}$ histograms have asymmetric tails extending toward the higher temperature (Fig. 2), and they are well fitted by the log-normal distribution:

$$\frac{1}{\sqrt{2\pi}\sigma T} \exp\left\{-\frac{(\log T - \mu)^2}{2\sigma^2}\right\}. \quad (22)$$

The mode temperature of the $T_{\max}^{X_{\text{reac}}}$ distribution is defined here as the effective reaction temperature (T_{reac}) for the reaction and is expressed as

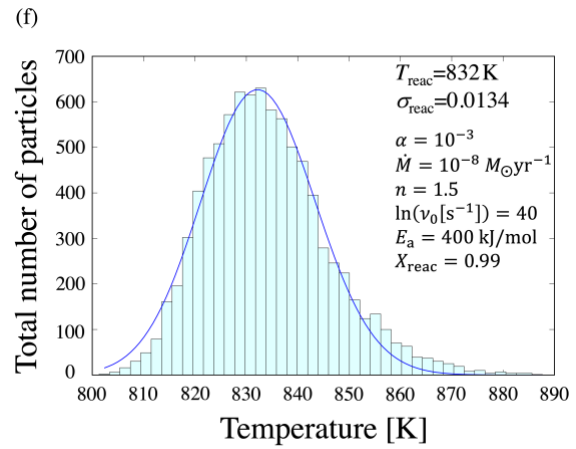
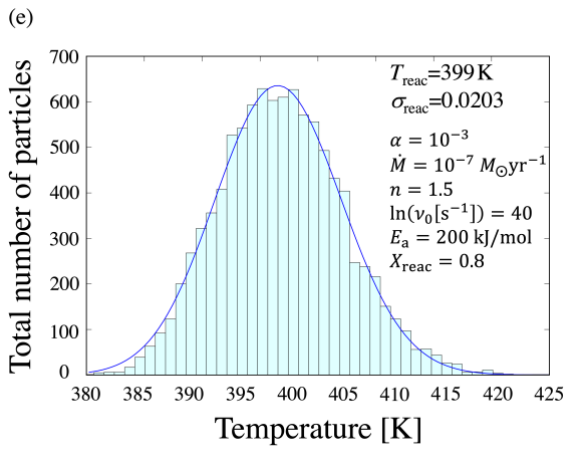
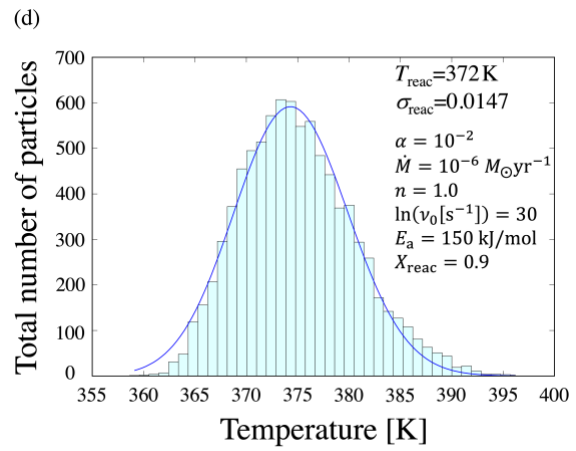
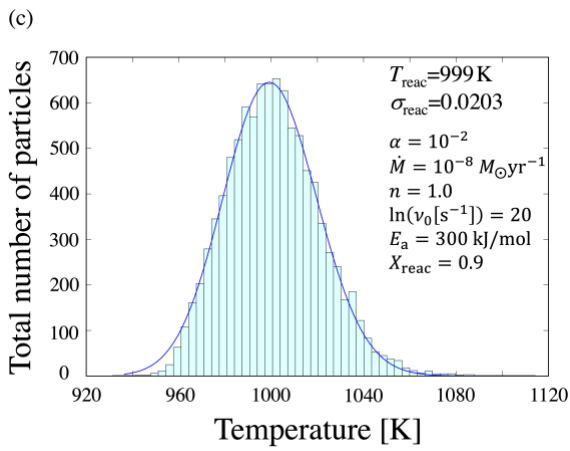
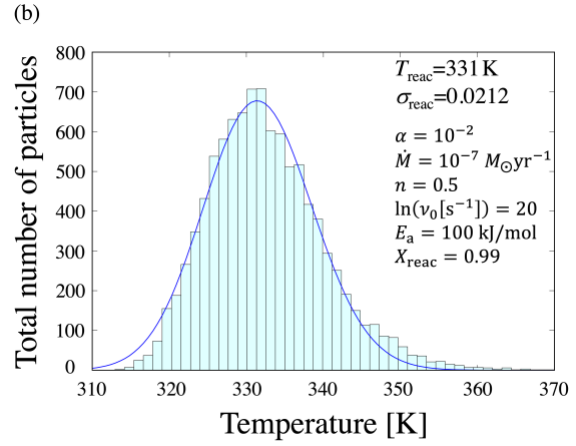
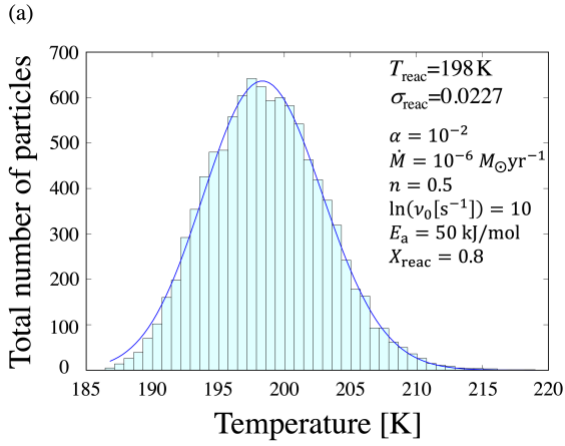
$$T_{\text{reac}} = \exp(\mu - \sigma^2). \quad (23)$$

The relative dispersion of T_{reac} is given as $\sigma_{\text{reac}} = \{e^{2\mu+\sigma^2}(e^{\sigma^2} - 1)\}^{1/2}/T_{\text{reac}}$. When $\sigma_{\text{reac}} \ll 1$, σ_{reac} nearly equals σ in Eq. (22). We found that σ_{reac} in all the simulations can be represented by σ . For instance, in the case of Fig. 2(a), T_{reac} of 1312 K and σ_{reac} of 0.0275 ($\ll 1$) are obtained.

The effective reaction temperatures (T_{reac}) and their relative dispersion (σ_{reac}) for various fictitious reactions vary depending on the reaction parameters and disk parameters (Fig. 3). We here note that the simulation results with T_{reac} of >1500 K are not used for further discussion because silicate dust sublimates at such high temperatures and the assumption of $\kappa=2.5$ cm²/g (Section 2) is no longer valid. The results with T_{reac} of <180 K or those with the $T_{\max}^{X_{\text{reac}}}$ distribution with a tail down to <180 K are also excluded because the dust release temperature was ~ 180 K in the numerical simulations, and the effect of the dust release location cannot be ignored. With those exceptions, T_{reac} obtained in the present simulation ranges from 188 to 1499 K, which covers various chemical reactions occurring in a wide range of temperatures.

As a natural consequence of temperature-dependent reactions, T_{reac} becomes larger as E_a increases or $\ln(\nu_{\text{chem}}[\text{s}^{-1}])$ decreases because the reactions require higher temperatures to proceed effectively with larger E_a and smaller ν_{chem} (Fig. 3). The σ_{reac} increases as $\ln(\nu_{\text{chem}}[\text{s}^{-1}])$ decreases but it does not depend largely on E_a (Fig. 3). The T_{reac} and σ_{reac} show weak dependence on the Avrami index n . They increase as n decreases (Fig. 3) because a reaction occurs effectively when X exceeds $1 - (1/e) \approx 0.632$ for a larger n .

As for the dependence on disk parameters, T_{reac} shows positive and negative correlation with α and \dot{M} , respectively, while σ_{reac} has little dependence on the disk parameters. The origins of these dependences/independences are shown through the derivation of the generalized formula in the next section.



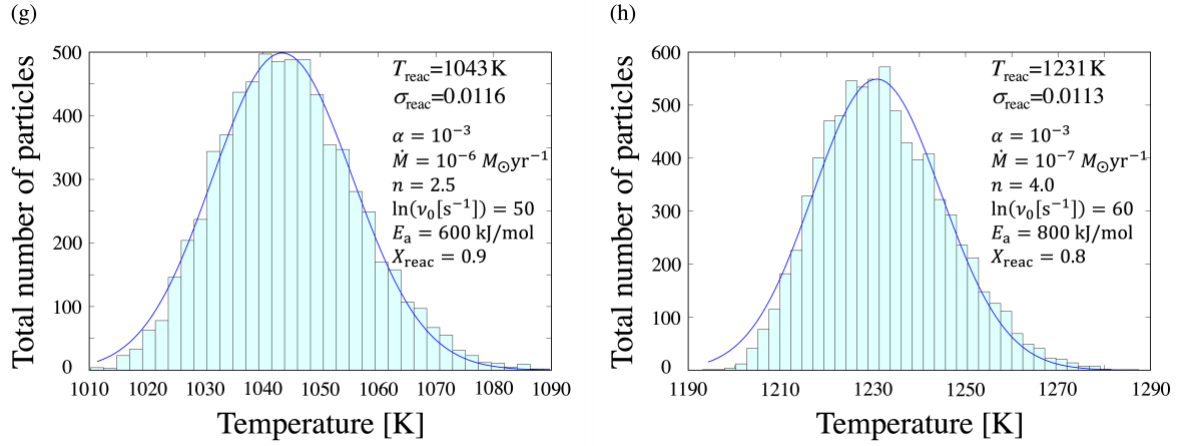


Figure 2. Histograms of $T_{\max}^{X_{\text{reac}}}$ (the highest temperature that a dust particle experiences before the reaction degree X reaches X_{reac}) of 10^4 particles in the simulations with different sets of reaction and disk parameters. The fitted curves with log-normal distributions (Eq.22) are also shown as solid curves.

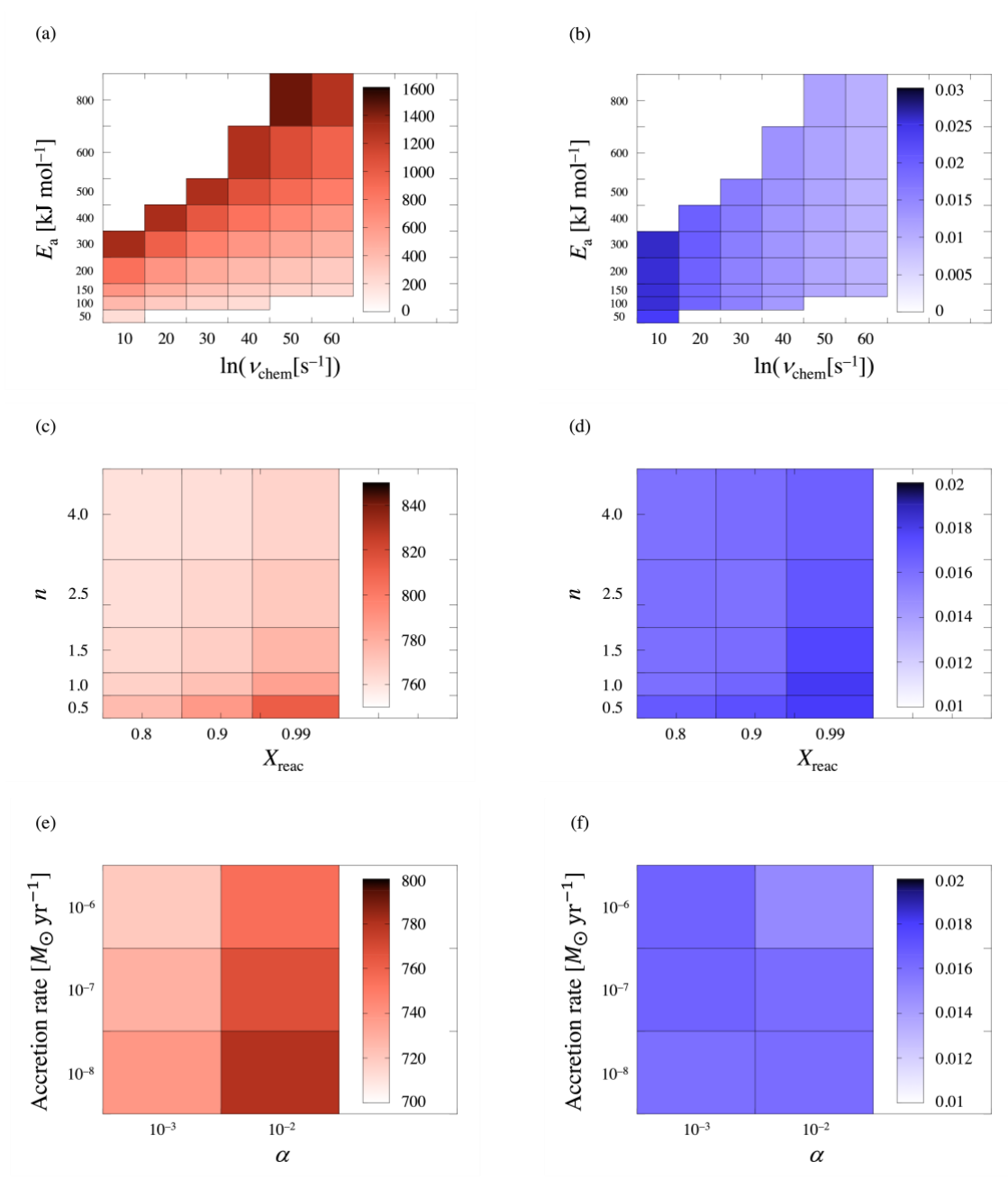


Figure 3. T_{reac} (K) [left panels] and its relative dispersion (σ_{reac}) [right panels] for the reactions with different reaction parameter sets (E_a , $\ln \nu_{\text{chem}}$, and n) in accretion disks (α and \dot{M}). (a) T_{reac} and (b) σ_{reac} for different E_a and $\ln(\nu_{\text{chem}}[\text{s}^{-1}])$ ($X_{\text{reac}}=0.9$, $n=1.5$, $\alpha=10^{-2}$, and $\dot{M} = 10^{-7} M_{\odot} \text{ yr}^{-1}$). (c) T_{reac} and (d) σ_{reac} for different Avrami indexes n and X_{reac} ($E_a=300 \text{ kJ mol}^{-1}$, $\ln(\nu_{\text{chem}}[\text{s}^{-1}])=30$, $\alpha=10^{-2}$, and $\dot{M} = 10^{-7} M_{\odot} \text{ yr}^{-1}$). (e) T_{reac} and (f) σ_{reac} for different disk parameters α and \dot{M} ($X_{\text{reac}}=0.9$, $E_a=300 \text{ kJ mol}^{-1}$, $\ln(\nu_{\text{chem}}[\text{s}^{-1}])=30$, $n=1.5$).

4. GENERALIZED FORMULA

4.1. Timescales of a chemical reaction and diffusive transport of dust

The reaction of a dust particle in the disk proceeds effectively when the dust particle stays in the region with a certain temperature range, which is high enough for the effective reaction, for a reasonably long duration before they leave the region. Therefore, comparison between a reaction timescale and a local diffusive transport timescale of dust particles is essential to discuss how T_{reac} (Figs. 2 and 3) is determined. We note that dust movement is driven by both advection and diffusion to the same degree; the advection velocity ($-3n_{\text{vis}}/2r$) gives the drift timescale of $\sim 2r^2/3n_{\text{vis}}$ that is almost the same as the diffusion timescale of $\sim r^2/n_{\text{vis}}$. Therefore, the diffusion timescale can be compared with the reaction timescale as a representative timescale of dust motion.

The reaction timescale is given here as a function of X and n by

$$t_X = \frac{1 - X}{|dX/dt|} = \frac{[-\ln(1 - X)]^{-(n-1)/n}}{n} \tau = C_X \tau \quad (24)$$

where τ is the characteristic timescale of a reaction (Eq. 16), and n is the Avrami index (Eq. 15). Equation (24) gives the time required for the completion of reaction from the reaction degree of X . C_X is larger than 1 and has positive dependence on X for $n < 1.0$, while it is smaller than 1 with negative X dependence for $n > 1.0$, which will be discussed later when a semi-analytical formula of T_{reac} is developed (Section 4.2).

The radial diffusion timescale for the radial scale Δr is expressed by:

$$t_{\text{diff}} \sim \frac{(\Delta r)^2}{v_{\text{vis}}} \simeq \alpha^{-1} \left(\frac{\Delta r}{r} \right)^2 \frac{v_K^2}{c_s^2} \Omega_K^{-1}, \quad (25)$$

where the local speed of sound c_s and the Kepler velocity v_K with a solar-mass central star are given by

$$c_s \simeq 1.83 \left(\frac{T_c}{10^3 \text{ K}} \right)^{1/2} \text{ km/s}, \quad (26)$$

$$v_K \simeq 29.8 \left(\frac{r}{1 \text{ au}} \right)^{-1/2} \text{ km/s}, \quad (27)$$

respectively. Because the midplane temperature is highest at a given r from the Sun and the most effective reaction is expected for the dust moving inward, the midplane temperature T_c is used to evaluate c_s .

By substituting Eqs. (26), (27), and (7) into Eq. (25), the diffusion timescale is expressed as:

$$t_{\text{diff}} \simeq 1.03 \times 10^7 \left(\frac{\alpha}{10^{-2}} \right)^{-10/9} \left(\frac{\dot{M}}{10^{-7} M_\odot \text{ yr}^{-1}} \right)^{2/9} \left(\frac{\Delta r/r}{0.01} \right)^2 \left(\frac{T}{10^3 \text{ K}} \right)^{-14/9} \text{ s}. \quad (28)$$

We evaluate $\Delta r/r$ in the following subsections.

4.2. Semi-analytical derivation of the effective reaction temperature and its dispersion

We here discuss semi-analytical formulas for the effective reaction temperature and its dispersion to reproduce the numerical results, by comparing the reaction and diffusion timescales of dust. The reaction timescale (Eq. 24) is rewritten as a logarithmic form using Eq. (16):

$$\ln(t_X) = \ln C_X + \ln(\tau [s]) = \ln C_X + \frac{E_a}{RT} - \ln(v_{\text{chem}} [s^{-1}]). \quad (29)$$

The diffusion timescale in Eq. (28) is also given as a logarithmic form:

$$\ln(t_{\text{diff}}) \simeq 16.15 - \frac{10}{9} \ln\left(\frac{\alpha}{10^{-2}}\right) + \frac{2}{9} \ln\left(\frac{\dot{M}}{10^{-7} M_{\odot} \text{ yr}^{-1}}\right) + 2 \ln\left(\frac{\Delta r/r}{0.01}\right) - \frac{14}{9} \ln\left(\frac{T}{10^3 \text{ K}}\right). \quad (30)$$

At the effective reaction temperature (T_{reac}), a chemical reaction proceeds efficiently before the dust diffuses out from the region of T_{reac} . From $\ln(t_X) = \ln(t_{\text{diff}})$, we obtain the effective reaction temperature of T_{reac} as follows:

$$T_{\text{reac}} = \frac{E_a}{R} \left[16.15 - \ln C_X + \ln(v_{\text{chem}} [s^{-1}]) - \frac{10}{9} \ln\left(\frac{\alpha}{10^{-2}}\right) + \frac{2}{9} \ln\left(\frac{\dot{M}}{10^{-7} M_{\odot} \text{ yr}^{-1}}\right) + 2 \ln\left(\frac{\Delta r/r}{0.01}\right) - \frac{14}{9} \ln\left(\frac{T}{10^3 \text{ K}}\right) \right]^{-1} \text{ K}. \quad (31)$$

Equation (31) shows that T_{reac} becomes higher for the larger X when $n < 1$ (Eq. 24), which is consistent with the numerical simulations that show the higher mode temperatures for the larger X_{reac} (Fig. 3). On the other hand, when n is larger than 1, the opposite trend is found for T_{reac} with C_X in Eq. (24). To avoid this inconsistency, we propose to use C_X of $1/n$ for $n > 1$. Because C_X (Eq. 24) does not show a strong dependence on X in the realistic ranges of n ($1 < n < 4$) and X (0.8–0.99), the approximation of C_X as $1/n$ for $n > 1$ is a reasonable assumption. In the discussion below, we use the following C_X ;

$$C_X = \frac{1}{n} [-\ln(1-X)]^{-(n-1)/n} \quad [\text{for } n < 1], \quad (32)$$

$$C_X = \frac{1}{n} \quad [\text{for } n \geq 1]. \quad (33)$$

Because the variation ranges of disk parameters (α , \dot{M} , $\Delta r/r$ and T) are narrower than those on the reaction parameters (v_{chem} , and C_X) and the E_a dependence is stronger than those of the other parameters, T_{reac} in Eq. (31) has weaker dependence on the disk parameters. Accordingly, a rough estimate of the effective reaction temperature is given by

$$T_0 = \frac{E_a}{R} [16.15 - \ln C_X + \ln(v_{\text{chem}} [s^{-1}])]^{-1} \text{ K}. \quad (34)$$

Substituting T_0 for T in the right-hand side of Eq. (31), T_{reac} is expressed by

$$T_{\text{reac}} = \frac{E_a}{R} \left[16.15 - \ln C_X + \ln(v_{\text{chem}} [s^{-1}]) - \frac{14}{9} \ln\left(\frac{T_0}{10^3 \text{ K}}\right) + 2 \ln\left(\frac{\Delta r/r}{0.01}\right) - \frac{10}{9} \ln\left(\frac{\alpha}{10^{-2}}\right) + \frac{2}{9} \ln\left(\frac{\dot{M}}{10^{-7} M_{\odot} \text{ yr}^{-1}}\right) \right]^{-1} \text{ K}. \quad (35)$$

The upper and lower lines of Eq. (35) express the dependences on the reaction parameters and the disk parameters, respectively, because T_0 and $\Delta r/r$ are determined only by the reaction parameters (Eqs. 34 and 38). The parameter, $\Delta r/r$, which is not fixed in Eq. (31), can be rewritten using the characteristic reaction timescale (Eq. (16)) and its relative dispersion ($\Delta \tau/\tau$) as

$$\frac{\Delta r}{r} = \left| \frac{\partial \ln r}{\partial \ln T} \frac{\partial \ln T}{\partial \ln \tau} \frac{\Delta \tau}{\tau} \right| = \frac{10 RT}{9 E_a} \left| \frac{\Delta \tau}{\tau} \right|, \quad (36)$$

where the relation,

$$\frac{\Delta T}{T} \approx \frac{1}{T} \frac{\Delta T}{\Delta r} \Delta r \approx \left| \frac{d \ln T}{d \ln r} \right| \frac{\Delta r}{r} = \frac{9}{10} \frac{\Delta r}{r}, \quad (37)$$

is used (Eq. (7)). Applying $T = T_0$ (Eq. 36), $\Delta r/r$ is given as

$$\frac{\Delta r}{r} = \frac{10}{9} \left| \frac{\Delta \tau}{\tau} \right| [16.15 - \ln C_X + \ln(\nu_{\text{chem}} [s^{-1}])]^{-1}. \quad (38)$$

The parameter $\Delta \tau/\tau$ should be empirically determined through comparison with the results of numerical simulations (Section 4.3).

The dispersion of the effective reaction temperature (σ_{reac}) is expected to be related to the temperature dispersion within Δr . Assuming that σ_{reac} is given simply by a linear function of $\Delta T/T$,

$$\sigma_{\text{reac}} = \frac{\Delta T_{\text{reac}}}{T_{\text{reac}}} = C_\sigma \frac{\Delta T}{T} = C_\sigma \left| \frac{\Delta \tau}{\tau} \right| [16.15 - \ln C_X + \ln(\nu_{\text{chem}} [s^{-1}])]^{-1}, \quad (39)$$

Where C_σ is a fitting parameter to explain σ_{reac} in the numerical simulations (Fig. 3).

4.3. Prediction formulas of the effective reaction temperature and its dispersion

The histograms of $T_{\max}^{X_{\text{reac}}}$ obtained in the numerical simulations are compared with the log-normal distributions using T_{reac} (Eq. 35) and σ_{reac} (Eq. 39) as a mode temperature (Eq. 23) and its dispersion (σ in the log-normal distribution; Eq. (22)), respectively. As described in the previous section, $\Delta\tau/\tau$ (Eq. 36) and C_σ (Eq. 39) are the free parameters, while it is most likely that they are of the order of $O(1)$ because the numerical simulations show that the reactions occur in limited temperature ranges depending on the reaction parameters.

Figure 4 compares the histograms of $T_{\max}^{X_{\text{reac}}}$ with predicted distributions of effective reaction temperatures with $\Delta\tau/\tau$ of 0.4 and C_σ of 1.8, which were determined by the least absolute value estimation. We found that the predicted distributions of T_{reac} with these values of $\Delta\tau/\tau$ and C_σ well explain the mode temperatures and their dispersion for the reactions in the numerical simulations with wide parameter ranges. The predicted mode temperature (T_{reac}) matches with those in the numerical simulation results within $\pm 5.5\%$ for all the range of reaction and disk parameters (Fig. A1). The relative dispersion of the reaction temperature σ_{reac} also well explain those obtained in the numerical simulations within $\pm 24\%$ (Fig. A2).

We thus conclude that the prediction formulas obtained in this study (Eqs. (35) and (39) with $\Delta\tau/\tau = 0.4$ and $C_\sigma = 1.8$) well reproduce the numerical simulation results for the irreversible reactions occurring in a wide range of disk temperature.

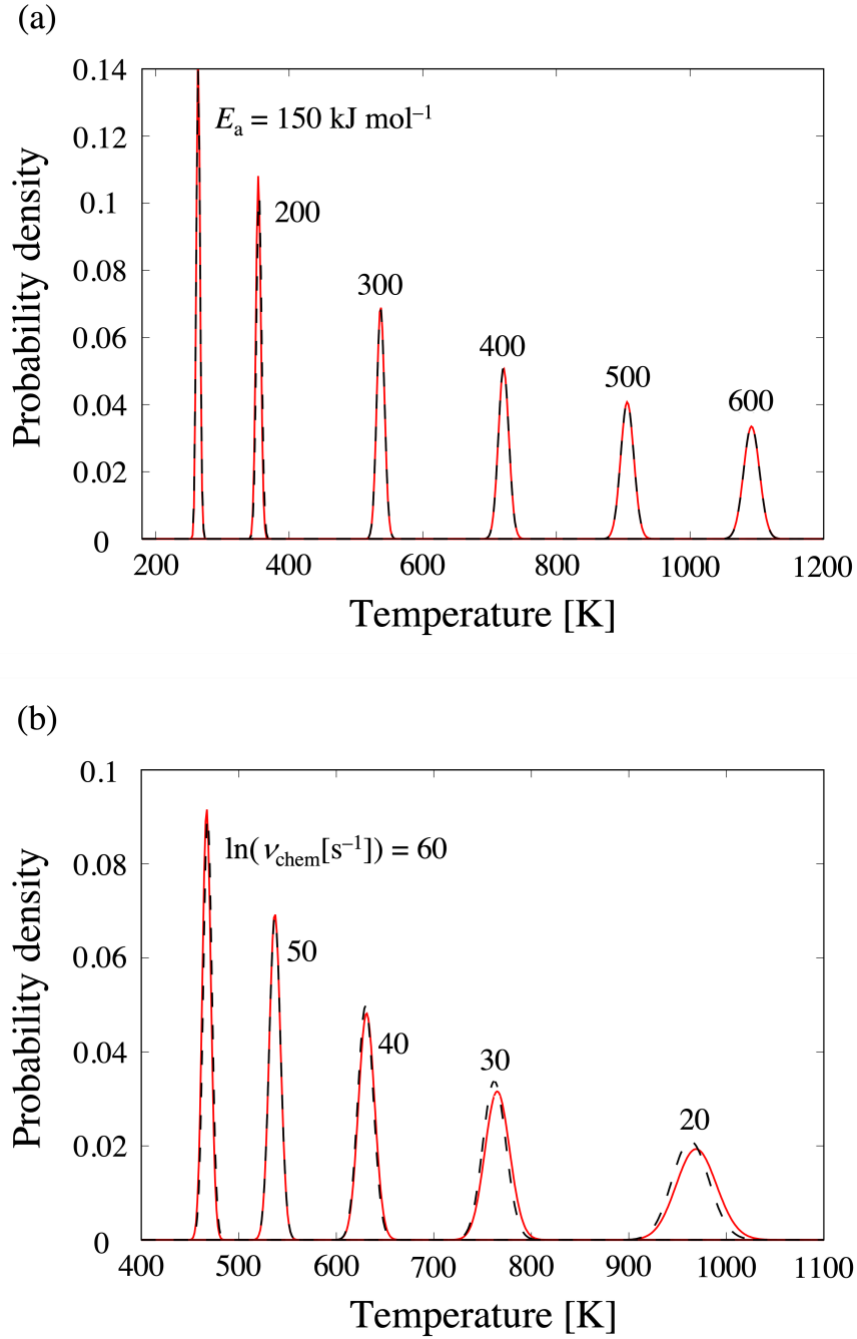


Figure 4. The histograms of $T_{\text{max}}^{X_{\text{reac}}}$ ($X_{\text{reac}}=0.99$) obtained in the numerical simulations for various chemical reactions (red solid curves) compared with the predicted distributions (black dashed curves; $\Delta\tau/\tau = 0.4$, $C_\sigma = 1.8$). (a) Reactions with different activation energies ($\ln(v_{\text{chem}}[\text{s}^{-1}]) = 50$ and $n = 1.5$). (b) Reactions with different pre-exponential factors ($E_a = 300 \text{ kJ mol}^{-1}$ and $n = 1.5$). The disk parameters are $\alpha=10^{-2}$ and $\dot{M}=10^{-6} M_\odot \text{ yr}^{-1}$.

5. APPLICATION OF PREDICTION FORMULAS FOR CRYSTALLIZATION AND OXYGEN ISOTOPE EXCHANGE OF AMORPHOUS SILICATE DUST AND ITS COSMOCHEMICAL IMPLICATIONS

In this section, we apply the prediction formula to evaluate the temperatures required for the crystallization of amorphous silicate dust and their oxygen isotope exchange with disk H₂O vapor.

It has been pointed out that Earth, Mars, chondrites, differentiated meteorites, asteroids (Itokawa and Ryugu), and a comet Wild 2 are depleted in ¹⁶O compared to the Sun (e.g., McKeegan et al., 2006, 2011; Yurimoto et al. 2008, 2011; Yokoyama et al., 2022). This difference in oxygen isotopic compositions between the Sun and the Solar System materials has been attributed to the oxygen isotope exchange between silicate dust and ¹⁶O-depleted H₂O vapor, which is likely to have formed through CO self-shielding (Yurimoto & Kuramoto 2004; Lyons & Young, 2005).

Yamamoto et al. (2018, 2020) experimentally determined the oxygen isotope exchange kinetics of amorphous magnesian silicate dust with H₂O vapor, controlled by oxygen isotope diffusion in the amorphous structure. They showed that the oxygen isotope exchange occurs for amorphous silicate dust more effectively than crystalline silicate dust, and discussed that the oxygen isotope exchange should occur at lower temperatures than the crystallization of amorphous silicate for the efficient oxygen isotope exchange. They found that there would be a temperature condition where such effective isotope exchange occurs prior to crystallization, but their discussion did not take the disk dynamics into consideration.

We converted the oxygen isotope exchange rate of sub-micron sized amorphous magnesian silicate dust (80 nm in diameter), having the forsterite (Mg₂SiO₄) stoichiometry (hereafter amorphous forsterite), with H₂O vapor in Yamamoto et al. (2018) into the JMA equation ($E_a = 161.4 \text{ kJ mol}^{-1}$; $\ln(n_{\text{chem}}[\text{s}^{-1}]) = 9.80$; $n = 0.67$) to evaluate the effective reaction temperature. We here note that the supply of H₂O may possibly control the exchange reaction at high temperatures (>800 K) and low H₂O pressure ($\sim 10^{-4}$ Pa) for (Yamamoto et al., 2018), but the obtained effective reaction temperatures are <800 K (see below) and thus we did not use the gas supply-controlled rate in this study.

The predicted effective temperature of the oxygen isotope exchange reaction ($X = 0.99$) and its dispersion are shown in Fig. 5. We also evaluated the effective crystallization temperature ($X = 0.99$) of amorphous silicate dust with the forsterite stoichiometry using the crystallization kinetics obtained by Yamamoto and Tachibana (2018) ($E_a = 414.4 \text{ kJ mol}^{-1}$; $\ln(n_{\text{chem}}[\text{s}^{-1}]) = 40.2$; $n = 1.5$) (Fig. 5). Yamamoto and Tachibana (2018) concluded that the crystallization of amorphous forsterite in vacuum is a diffusion-controlled reaction within the grain. They found that the reaction parameters change with the partial pressure of H₂O vapor. However, its dependence is not significant enough within the range of disk parameters in this study, and those in vacuum are appropriate to be applied in this work.

We found that crystallization of the amorphous forsterite dust occurs in the temperature range of 800–925 K, while oxygen isotope exchange for 80 nm-sized dust completes at 650–800 K under different sets of disk parameters (Fig. 5). Irrespective of disk parameters, the effective temperatures of two reactions do not overlap each other even considering the reaction temperature dispersions. We also made the 3D Monte Carlo simulation (Section 2) for 10^4 particles using the reaction parameters above (Yamamoto et al. 2018; Yamamoto & Tachibana 2018) and confirmed that the prediction formulas well represent T_{reac} and s_{reac} obtained in the numerical simulations (Fig. 5).

Yamamoto and Tachibana (2018) found that amorphous forsterite dust crystallizes in 10^6 , 10^4 , 10^2 , and 1 yr at ~ 700 , ~ 760 , ~ 820 , and ~ 880 , respectively, based on the reaction kinetics. Similarly, Yamamoto et al. (2018) showed that 80 nm-sized amorphous forsterite dust can completely exchange oxygen isotope with H_2O vapor for 10^6 , 10^4 , 10^2 , and 1 yr at ~ 510 , ~ 580 , ~ 675 , and ~ 800 K, respectively. However, the realistic temperature-time ranges of dust in the protoplanetary disk could not be discussed only from the reaction rates. The effective temperatures for the oxygen isotope exchange and crystallization of sub-micron amorphous forsterite in this work are 650–800 and 800–925 K, respectively. These temperature ranges correspond to the characteristic reaction timescales of ~ 1 –100 yr for oxygen isotope exchange and ~ 0.1 –1 yr for crystallization, which can be determined only by comparing the timescales of reactions and dust dynamics in the protoplanetary disk.

The present results (Fig. 5) suggest that sub-micron sized amorphous forsterite dust completes the oxygen isotope exchange with the disk H_2O vapor prior to its crystallization in the accreting disk. Further discussion on the dust grain size, the presence of other gas species (e.g., CO), and the chemical composition of amorphous silicate dust, all of which affect the oxygen isotope exchange reaction of dust (e.g., Yamamoto et al., 2018, 2020), is needed, but this work showed the first quantitative discussion on the oxygen isotope evolution of amorphous silicate dust in the protosolar disk.

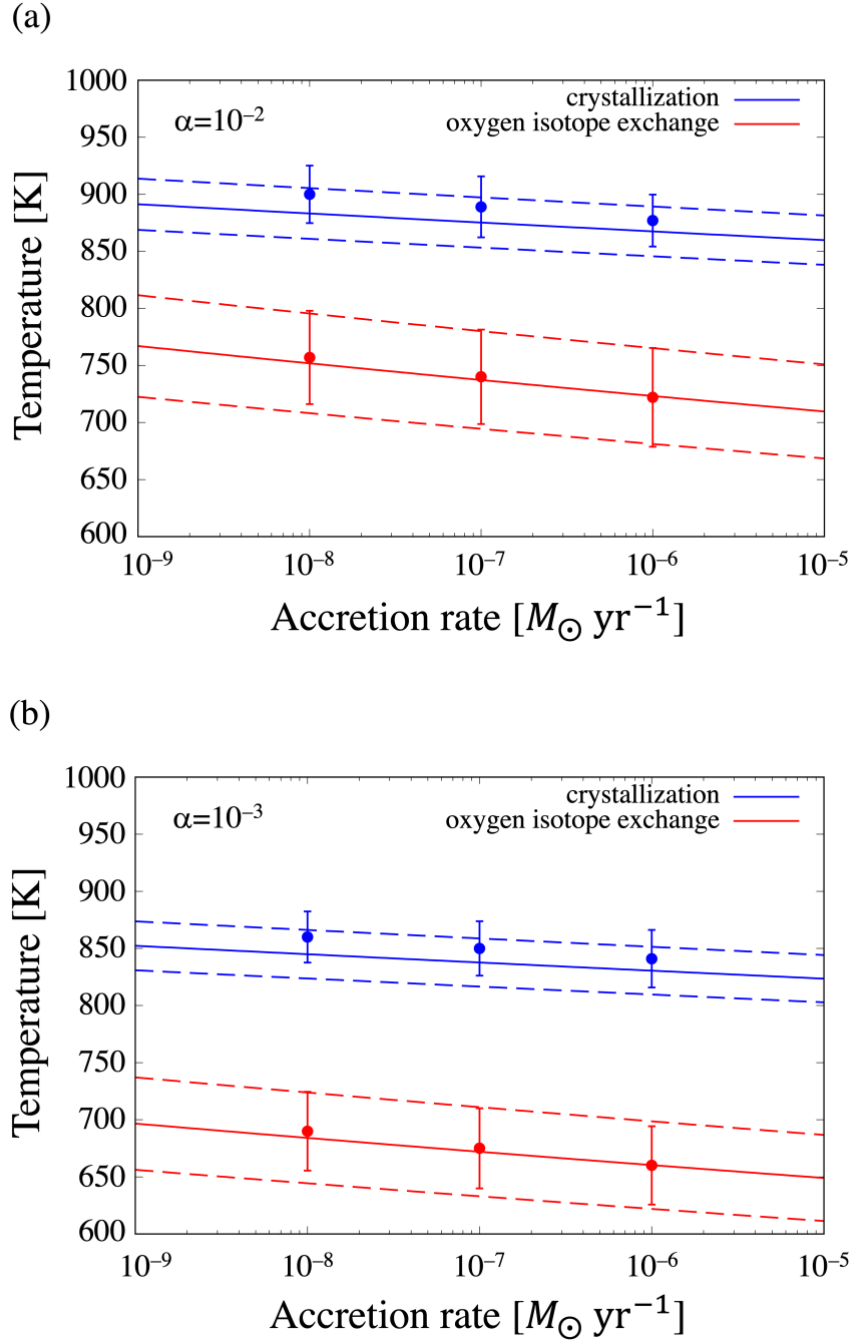


Figure 5. The effective reaction temperatures, derived from Eq. (35), for crystallization (blue solid curves) and oxygen isotope exchange (red solid curves) for amorphous forsterite in steady accretion disks with $\alpha=10^{-2}$ and 10^{-3} . Dispersions of reaction lines (Eq. (39)) are plotted as dashed curves. Solid circles represent $T_{\text{max}}^{\text{X}_{\text{reac}}}$ ($X_{\text{reac}}=0.99$) and its dispersion (error bars) obtained by the Monte Carlo simulation (blue: crystallization; red: oxygen isotope exchange).

6. CONCLUSIONS

In this study, we performed 3D Monte Carlo simulations of various irreversible chemical reactions of dust particles drifting and diffusing in a steady accretion disk to determine the effective reaction temperatures. We adopt the r - z disk temperature determined by viscous heating of which rate is proportional to gas density and inject amorphous submicron-sized silicates at the snow line on the midplane of the disk, following Okamoto and Ida (2022).

The simulations with 5940 parameter sets (6 disk conditions x 330 chemical reactions x 3 reaction degrees) showed that the highest temperatures ($T_{\max}^{X_{\text{reac}}}$) that individual particles experience before the reaction reaches a certain degree show distributions that can be fitted by the log-normal distribution. The mode temperature and the dispersion of the $T_{\max}^{X_{\text{reac}}}$ distribution depend on the reaction and disk parameters, and the mode temperature is defined as the effective reaction temperature.

We developed the semi-analytical prediction formulas of the effective reaction temperature and its dispersion by comparing the reaction timescale with the diffusive transport timescale of dust particles:

$$T_{\text{reac}} = \frac{E_a}{R} \left[16.15 - \ln C_x + \ln(v_{\text{chem}} [s^{-1}]) + 2 \ln \left(\frac{\sigma_{\text{reac}}}{0.0162} \right) - \frac{14}{9} \ln \left(\frac{T_0}{10^3 \text{ K}} \right) - \frac{10}{9} \ln \left(\frac{\alpha}{10^{-2}} \right) + \frac{2}{9} \ln \left(\frac{\dot{M}}{10^{-7} M_{\odot} \text{ yr}^{-1}} \right) \right]^{-1} \text{ K}, \quad (40)$$

where C_x is a parameter related to the reaction (Eqs. 32 and 33) and T_0 is determined only by the reaction parameters (Eq. 34). The upper and lower lines of Eq. (40) express the dependences on the reaction parameters and the disk parameters, respectively. The relative dispersion of the reaction line (σ_{reac}) is given by

$$\sigma_{\text{reac}} = 0.72 \times [16.15 - \ln C_x + \ln(v_{\text{chem}} [s^{-1}])]^{-1}. \quad (44)$$

These prediction formulas of the effective reaction temperature and its dispersion well explain the results of numerical simulations in a wide range of reaction temperatures (~ 200 – 1400 K) within $\pm 5.5\%$ and $\pm 24\%$, respectively.

We applied the prediction formulas for oxygen isotope exchange and crystallization of sub- μm sized amorphous silicate dust with the forsterite composition based on experimentally determined reaction rates. It was found that oxygen isotope exchange of amorphous forsterite dust with H_2O vapor completes before the dust crystallizes in the disk. This would result in effective oxygen isotope evolution of silicate dust in the Solar System and may explain the oxygen isotope difference of planetary materials from the Sun.

These prediction formulas make it possible to discuss various chemical reactions, of which kinetics is obtained in laboratory experiments, in accreting protoplanetary disks without making numerical simulations, and are a powerful tool to understand distributions of materials that experience different chemical processes in protoplanetary disks.

7. ACKNOWLEDGEMENTS

We thank Aki Takigawa for fruitful discussion and two anonymous reviewers for their helpful comments and suggestions. This work is supported by the KAKENHI grant 19H00712, 20H05846, 21H04512, and 21K13986.

APPENDIX

DISK VERTICAL TEMPERATURE DISTRIBUTION

With the diffusion approximation, the vertical radiative flux F is given by

$$F = -\frac{4\sigma_B}{3\kappa\rho} \frac{dT^4}{dz}, \quad (\text{A1})$$

where σ_B is Stefan-Boltzmann constant. Assuming the optically thick region ($\tau \gtrsim 1$), the flux satisfies

$$\frac{dF}{dz} = q_{\text{vis}} = \frac{9}{4} \rho v_{\text{vis}} \Omega_K^2, \quad (\text{A2})$$

where q_{vis} is the viscous heating source.

The flux F must be radiated away at $z \sim z_s$. The integration of Eq. (A1) from $z = -z_s$ to $z = z_s$, using approximation of $\int_{-z_s}^{z_s} \rho dz \sim \int_{-\infty}^{\infty} \rho dz$ because $z_s \sim$ a few H , is

$$F(z_s) - F(-z_s) = \int_{-z_s}^{z_s} \frac{9}{4} \rho v_{\text{vis}} \Omega_K^2 dz \simeq \frac{9}{4} v_{\text{vis}} \Omega_K^2 \int_{-\infty}^{\infty} \rho dz = \frac{9}{4} \Sigma_z v_{\text{vis}} \Omega_K^2, \quad (\text{A3})$$

Because $F(z_s) - F(-z_s) = 2F(z_s) = 2\sigma_B T_s^4$ and $S_g n_{\text{vis}} W_K^2 = \dot{M}/3\pi$, the photosurface temperature is given by

$$\sigma_B T_{\text{surf}}^4 \simeq \frac{9}{8} \Sigma_z v_{\text{vis}} \Omega_K^2 = \frac{9}{8\pi} \dot{M} \Omega_K^2, \quad (\text{A4})$$

Which is explicitly expressed by Eq. (3):

$$T_{\text{surf}} \simeq 85 \left(\frac{\dot{M}}{10^{-8} M_{\odot}/\text{yr}} \right)^{1/4} \left(\frac{M_*}{M_{\odot}} \right)^{1/4} \left(\frac{r}{1\text{au}} \right)^{-3/4}. \quad (\text{A5})$$

Integrating Eq. (A1) from z to z_s ($z < z_s$),

$$\int_z^{z_s} \frac{3\kappa F}{4\sigma_B} \rho(z) dz = - \int_z^{z_s} d(T^4) = T(z)^4 - T_{\text{surf}}^4. \quad (\text{A6})$$

In this paper, the viscous heating is assumed to be proportional to $r(z)$. From Eq. (A6),

$$T(z)^4 - T_{\text{surf}}^4 = \int_z^{z_s} \frac{3\kappa F}{4\sigma_B} \rho(z) dz = - \frac{3}{4\sigma_B} \int_z^{z_s} F(z) d\tau. \quad (\text{A7})$$

From Eqs. (A2) and (A4) with an assumption that the opacity k does not depend on z ,

$$\frac{dF}{dz} = -\frac{9v_{\text{vis}}}{4\kappa} \Omega_K^2 = -\frac{9 \times 3\pi \Sigma_g v_{\text{vis}}}{4 \times 3\pi \Sigma_g \kappa} \Omega_K^2 = -\frac{3\dot{M}}{4\pi \tau_{\text{disk}}} \Omega_K^2 = -\frac{2\sigma_B}{\tau_{\text{disk}}} T_{\text{surf}}^4. \quad (\text{A8})$$

Equation (A8) is analytically integrated from 1 to t_z ,

$$(\tau_z - 1) \frac{2\sigma_B T_{\text{surf}}^4}{\tau_{\text{disk}}} = - \int_1^{\tau_z} \frac{dF}{d\tau} d\tau = -F + \sigma_B T_{\text{surf}}^4. \quad (\text{A9})$$

Substituting Eq. (A9) into Eq. (A7), we obtain

$$T(\tau_z)^4 - T_{\text{surf}}^4 = \frac{3}{4} \int_1^{\tau_z} T_{\text{surf}}^4 \left[1 - \frac{2(\tau_z - 1)}{\tau_{\text{disk}}} \right] d\tau = T_{\text{surf}}^4 \times \frac{3(\tau_z - 1)}{4} \left(1 - \frac{\tau_z - 1}{\tau_{\text{disk}}} \right). \quad (\text{A10})$$

Therefore, temperature at z is given by Eq. (4):

$$T(z) = \left[1 + \frac{3(\tau_z - 1)}{4} \left(1 - \frac{\tau_z - 1}{\tau_{\text{disk}}} \right) \right]^{1/4} T_{\text{surf}}. \quad (\text{A11})$$

DIFFERENCES IN THE PREDICTED REACTION TEMPERATURES AND THEIR DISPERSION FROM THE NUMERICAL SIMULATIONS

Examples of the deviation of the predicted effective reaction temperatures and their dispersion from those obtained in the numerical reaction is summarized in Figs. A1 and A2.

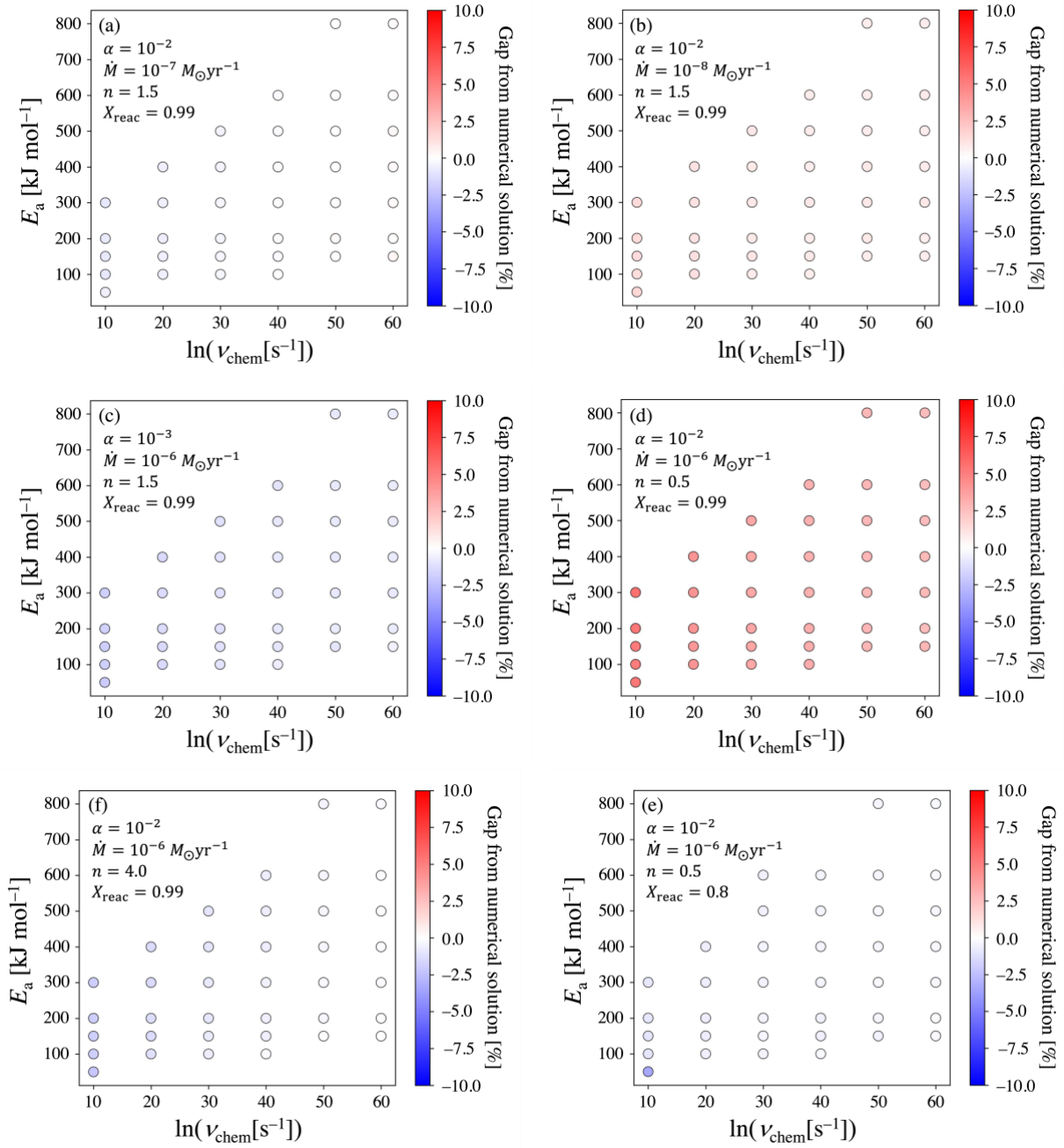


Figure A1. Deviation of the predicted effective reaction line temperatures from those obtained in the numerical simulations.

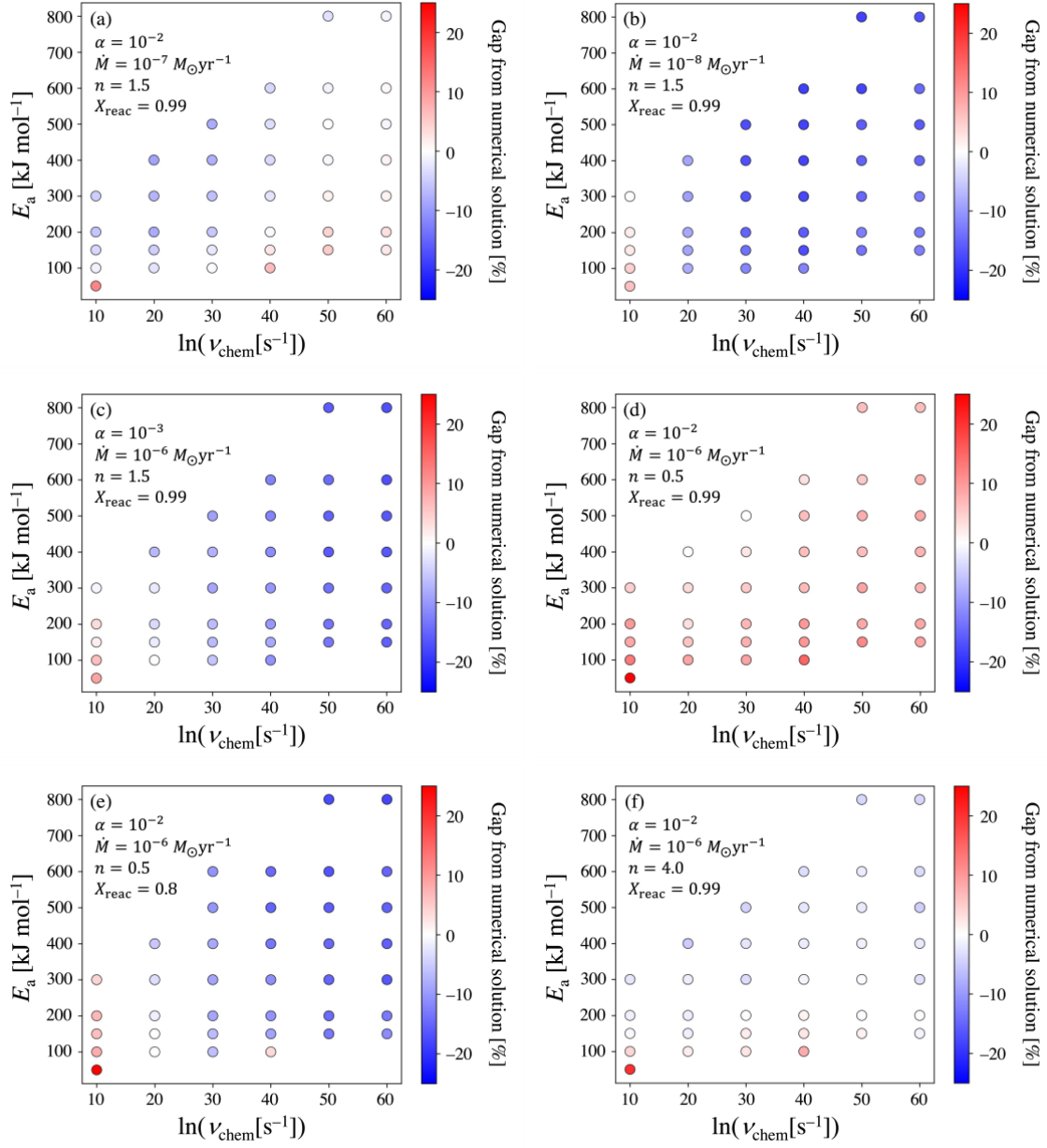


Figure A2. Deviation of the relative dispersion of the effective reaction temperatures from those obtained in the numerical simulations.

References

- Avrami, M. 1939, *J. Chem. Phys.*, 7, 1103
- Ciesla, F. J. 2010, *ApJ*, 723, 514
- Ciesla, F. J. 2011, *ApJ*, 740, 9
- Ciesla, F. J. and Sandfors. S. A., 2012, *Science*, 336, 452
- Dullemond, C. P., Apai, D., & Walch, S. 2006, *ApJ*, 640, L67
- Gail, H. P. 2001, *A&A*, 378, 192
- Ida, S., & Guillot, T., 2016, *A&A*, 596, L3
- Johnson, W. A., & Mehl, R. F. 1939, *Trans. AIME*, 135, 416
- Kuroda, M., Tachibana, S., Sakamoto, N. et al. 2018, *Am. Mineral.* 103, 412
- Kuroda, M., Tachibana, S., Sakamoto, N., & Yurimoto, H. 2019, *Am. Mineral.* 104, 385
- Lambrechts, M., & Johansen, A. 2014, *A&A*, 572, A107
- Lin & Papaloizou 1985, *PPII*, 981
- Lyons, J. R., & Young, E. D. 2005, *Nature*, 435, 7040
- McKeegan, K. D., Aleon, J., Bradley, J., et al. 2006, *Science*, 314, 1724
- McKeegan, K. D., Kallio, A. P. A., Heber, V. S., et al. 2011, *Science*, 332, 1528
- Morbidelli, A., Lambrechts, M., Jacobson, S., & Bitsch, B. 2015, *Icarus*, 258, 418
- Muzerolle, J. et al. 2000, *ApJ*, 535, L47
- Okamoto, T., & Ida, S. 2022, *ApJ*, 928, 171
- Pollack, J. B., McKay, C. P., & Christofferson, B. M., 1985, *Icarus*, 64, 3, 471
- Pollack, J. B. et al. 1994, *ApJ*, 421, 615.
- Saito, E., & Sirono, S. 2011, *ApJ*, 728, 20
- Sano T. et al. 2004, *ApJ*, 605, 321.
- Scott, D. W. 1979, *Biometrika*, 66, 3, 605
- Shakura, N. I., & Sunyaev, R. A. 1973, *A&A*, 24, 337
- Tachibana, S. & Tsuchiyama, A. 1998, *Geochim. Cosmochim. Acta* 62, 2005
- Tachibana, S., Tsuchiyama, A., & Nagahara, H. 2002, *Geochim. Cosmochim. Acta* 66, 713
- Tachibana, S., Nagahara, H., Ozawa, K., et al. 2011, *ApJ*, 736, 16
- Takigawa, A., Tachibana, S., Nagahara, H., et al. 2009, *ApJ*, 707, L97
- Takigawa, A., Tachibana, S., Nagahara, H., & Ozawa, K. 2015, *ApJS*, 218, 16
- Tsuchiyama, A., Tachibana, S., Takahashi, T. 1999, *Geochim. Cosmochim. Acta* 63, 2451
- Yamamoto, D., & Tachibana, S. 2018, *ESC*, 2, 778
- Yamamoto, D., Kuroda, M., Tachibana, S., Sakamoto, N., & Yurimoto, H. 2018, *ApJ*, 865, 98
- Yamamoto, D., Tachibana, S., Kawasaki, N., & Yurimoto, H. 2020, *Meteorit. Planet. Science*, 55, Nr 6, 1281
- Yamamoto, D., Kawasaki, N., Tachibana, S. et al. 2021, *Geochim. Cosmochim. Acta*, 314, 108
- Yokoyama et al., 2022, *Science*, abn7850.
- Yurimoto, H., & Kuramoto, K. 2004, *Science*, 305, 1763

Yurimoto, H., Krot, A. N., Choi, B., Alon, J., Kunihiro, T., & Brearley, A. J. 2008, *Rev. Mineral. Geochem.*, 68, 1, 141

Yurimoto, H. et al. 2011, *Science*, 333, 1116.